Check for updates

Superb adsorption capacity of biochar derived from leather shavings for Congo red†

Xueping Huang, Fan Yu, Qifan Peng and Yaqin Huang (ID) *

Research on biochar for removal of dyes has been a hot topic because of its excellent eco-friendly and economical properties. In this study, leather shavings biochar (LSB) with high adsorption capacity was prepared and tested with Congo red as a model dye for adsorption. The research results show that the as-prepared biochar exhibits a porous structure, with a high specific surface area (2365 m^2 g^{-1}), and it would be beneficial for removing Congo red from effluents. More interestingly, adsorption capacity of LSB for Congo red was enhanced by chromium compounds on the surface of biochar through chelation and electrostatic interactions. Chelation occured between the chromium compounds and amino groups of Congo red. Adsorption data for Congo red on the biochar were successfully described by Langmuir isotherm and the pseudo-second order kinetics model. Langmuir maximum adsorption capacity of LSB at 30 °C reached 1916 mg g^{-1}, which is much higher than that of conventional activated carbon (AC). Recycling experiment shows that LSB has a potential market for removing Congo red.

Introduction

Water is crucial for life and human social development. However, there are large quantities of dye effluents from textile, leather, paper, rubber, plastic, and dye manufacturing industries.[1] Toxic diazo dyes pose a serious risk to the ecosystem and even human health. Nowadays, Congo red (1-naphthalene sulfonic acid, 3,30-(4,40-biphenylenebis(azo)) bis(4-amino-)disodium salt, $C_{32}H_{22}N_6O_6S_2Na_2$, CR) is still a typical anionic diazo dye extensively used in industries due to its excellent surface adhesion and inexpensiveness.[2] CR, a well-known carcinogen and can be metabolized to benzidine, causes an allergic reaction.[3] Various types of water-treatment techniques, including adsorption,[4] coagulation,[5] photodegradation,[6] chemical oxidation[7] and electrochemical oxidation,[8] have been reported. Among these techniques, adsorption is an efficient and convenient way to remove dyes. Many advanced adsorbents are constantly being developed.[9–14]

Biochar, a solid carbonaceous product of biomass carbonization with little or no oxygen,[15] has received much attention due to its abundant surface pores and functional active sites. Feedstock for biochar includes vermicompost,[16] Korean cabbage waste,[4] poplar catkins,[17] durian rind,[18] rice straw,[19] bamboo,[20] palm oil[21] rice husks,[21] and cattle manure.[22] Moreover, achieving specific surface area and high adsorption capacity is always important in development of an efficient adsorbent.[23] Therefore, we focused on leather shavings, containing Cr_2O_3 disposed from tanning industries, as adsorbents. First, leather shavings are waste matter, whose handling is challenging for the manufacturers. The usage of this waste may contribute to disposal management of disposal, which is in agreement with the "3R" principles, "reduce, reuse and recycle". Second, metallic compounds show excellent adsorption capacity for CR, such as MgO/SiO_2,[24] Al_2O_3,[25] $CaCO_3$,[23] and ZnO-modified compounds.[10] Moreover, $-NH_2$ groups is typically present as a functional group in adsorbents for the adsorption of heavy metals.[26–28] This indicates that we can effectively the chromic oxide content in the leather shavings for the adsorption of CR, which has $-NH_2$ groups. Lastly, cost of metallic compounds usually limits their use as adsorbents, while leather shavings are cheap and abundant disposals.

Therefore, in this study, chromium-containing biochar from leather shavings was fabricated. This leather shavings biochar (LSB) exhibited superb adsorption capacity for removing CR from aqueous solution. Adsorption process of LSB well-fitted with the Langmuir isotherm and the pseudo-second order kinetics model. Results of X-ray photoelectron spectroscopy (XPS), Fourier transform infrared (FT-IR) spectroscopy, and the comparison of adsorption of Congo red and Methyl orange indicated that the reaction between chromium and CR plays an important role in the adsorption process. Thus, LSB would be a promising candidate for practical applications.

Beijing Laboratory of Biomedical Materials, Beijing Key Laboratory of Electrochemical Process and Technology for Material, Beijing University of Chemical Technology, Beijing, 100029, China. E-mail: huangyq@mail.buct.edu.cn

Experimental

Materials

CR (analytical reagent) used in this study was purchased from Tianjin Fu Chen Chemical Reagent Factory, China.

Hydrochloric acid (HCl, 35.0–37.0%), potassium hydroxide (KOH, 98.0%) and sodium hydroxide (NaOH, 98.0%) were purchased from Beijing Chemical works, China. Activated carbon (AC) used in this study was purchased from Sinopharm Chemical Reagent Co., Ltd (Shanghai, China).

Biochar preparation

Leather shavings obtained from the industry were oven-dried at 60 °C, and then crushed and pretreated in air to eliminate impurities from the leather and introduce oxygen. The obtained fragments were first pre-carbonized at a specific temperature for 1 h using a tube furnace (ZSK 1200, Beijing, China). After pre-carbonization, the obtained products were mixed with KOH at weight ratio 1 : 1, followed by carbonization process at different temperatures (750 °C and 900 °C) under nitrogen condition. Heating rate was adjusted to 10 °C min^{-1} and temperature was maintained at the peak for 1 h for complete carbonization. Finally, the leather shavings biochar was washed with boiled deionized water seven times to remove the activator and then dried in an oven. The biochar samples obtained according to the carbonization temperatures were labeled as LSB750 and LSB900.

Sample characterization

Surface morphologies of the adsorbents were characterized by scanning electron microscopy (SEM) using HITACHI S-4800. Energy dispersive spectroscopy (EDS) results were obtained using a scanning electron microscope (FEI Quanta650). N$_2$ adsorption–desorption isotherms were obtained on a Micromeritics ASAP 2020 instrument. Specific surface area and pore size distribution were calculated by Brunauer–Emmett–Teller (BET) and Non-Local Density Functional Theory (NLDFT) methods, respectively. X-ray diffraction (XRD) patterns were recorded using a D/max 2500 V X-ray diffractometer. Elemental compositions and binding energies of the adsorbents were determined using X-ray photoelectron spectroscopy (XPS, Thermo Fisher Scientific USA ESCALAB-250) and XPS Peak program (for spectra evaluation). Fourier transform infrared (FT-IR) spectroscopy was performed in the range of 400–4000 cm^{-1}.

Adsorption experiments

Batch experiments were carried out with the LSBs (LSB750 and LSB900) and AC. Specific dye concentrations of CR were prepared and ~10 mg adsorbent was weighed. Then, both were added into a 25 mL vial with a stopper. First, the influence of aqueous pH ranging from 6 to 10 was investigated. Adsorption isotherms were obtained, for the batch experiments using a thermostatic shaker at the initial pH. Influence of temperature was evaluated by adjusting the temperature at three different values: 30 °C, 40 °C and 50 °C. Once equilibrium was established, suspensions were centrifuged for 3 minutes at 10 000 rpm, and the supernatant was used to analyze dye concentration.

Adsorption isotherm models

In order to determine the CR adsorption ability of the adsorbents during the adsorption process, two well-known parameter-based equilibrium isotherm models, the Langmuir and Freundlich models, were applied.

Equilibrium adsorption capacity of the adsorbents for CR was calculated by eqn (1):

$$q_e = V \times (C_0 - C_e)/m \qquad (1)$$

where q_e (mg g^{-1}) is the amount of adsorbate adsorbed at equilibrium, C_0 (mg L^{-1}) and C_e (mg L^{-1}) are CR concentrations of the initial and equilibrium aqueous phases, respectively, V (L) is the volume of solution, and m (g) is the mass of adsorbent. C_e (mg L^{-1}) was determined using a UV-vis spectrometer (TU-1810, Beijing, China) at 497 nm for CR.

Langmuir isotherm, describing the adsorption on planar surfaces as well as monolayer adsorption, is given by eqn (2):

$$C_e/q_e = C_e/q_m + 1/(k_L q_m) \qquad (2)$$

where q_m (mg g^{-1}) is the maximum amount of CR adsorbed, and k_L (L mg^{-1}) is the sorption equilibrium constant.

Freundlich model, describing the adsorption on heterogeneous surfaces and multilayer adsorption, is expressed by eqn (3):

$$\log q_e = \log k_F + 1/n \log C_e \qquad (3)$$

where k_F (mg g^{-1}) is the relative adsorption capacity, and n is a parameter related to linearity.

Adsorption kinetic models

To evaluate the rate controlling mechanism of CR adsorption onto the adsorbents, two kinetic models were applied. Lagergren pseudo-first order kinetics model is given by eqn (4):

$$\log(q_e - q_t) = \log q_e - k_1 t/2.303 \qquad (4)$$

The Lagergren pseudo-second order kinetics model is described by eqn (5):

$$t/q_t = 1/k_2 q_e^2 + t/q_e \qquad (5)$$

where q_t (mg g^{-1}) represents amount of adsorbate adsorbed at a predetermined time, t (min), k_1 (min^{-1}) is the pseudo-first order rate constant, and k_2 (g mg^{-1} min^{-1}) is the pseudo-second order rate constant.

The effect of intraparticle diffusion resistance on adsorption can be evaluated by the eqn (6):

$$q_t = k_{id} t^{1/2} + I \qquad (6)$$

where k_{id} (mg g^{-1} min$^{1/2}$) is the rate constant of intraparticle diffusion. Values of I provide the information regarding the thickness of boundary layer.

Results and discussion

Morphologies of LSBs

Scanning electron microscopy (SEM) was used to reveal the structures of LSBs. As shown in Fig. 1a, surface of AC is intact
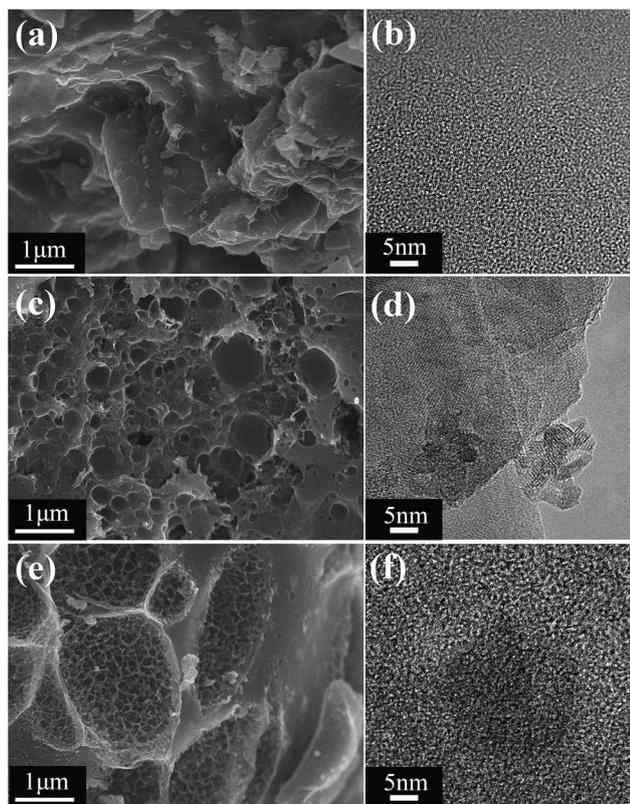
Fig. 1 (a, c and e) SEM images and (b, d and f) TEM images of (a and b) AC, (c and d) LSB750 and (e and f) LSB900.

and smooth, while LSB750 (Fig. 1c) and LSB900 (Fig. 1e) show a rough porous surfaces. The porous structure of LSB suggested a larger surface area than that of AC for dye interaction.[29] EDS mapping (Fig. S1†) demonstrates that the elements in LSBs are mainly C, Cr and O. The elemental mapping demonstrates the homogeneous distribution of chromium on the surface of biochar, with crystalline structures, which is consistent with the transmission electron microscopy (TEM) results for LSB750 (Fig. 1d) and LSB900 (Fig. 1f). Pore density of LSB slightly increased upon increasing the carbonization temperature from 750 °C to 900 °C; however, both surfaces were neatly arranged and interconnected. These large-scale pores were conducive to mass diffusion.[13] This indicated that the transfer of Congo red into porous adsorbents might occur.

Structure of LSBs

Specific surface area and porosity of LSBs and AC were studied by nitrogen adsorption–desorption measurements (Fig. 2a and S2a†). According to the IUPAC classification,[30] isotherms of the materials conform to the typical type I isotherm, which is inclined to the Y axis at the low-pressure region, indicating a microporous or micro-approximately mesoporous structures. The fast-growing nitrogen adsorption curves indicated molecular monolayer adsorption or microporous multilayer adsorption. After $P/P_0 > 0.4$, a hysteresis loop was observed for LSB900, where capillary condensation and inhomogeneous adsorption
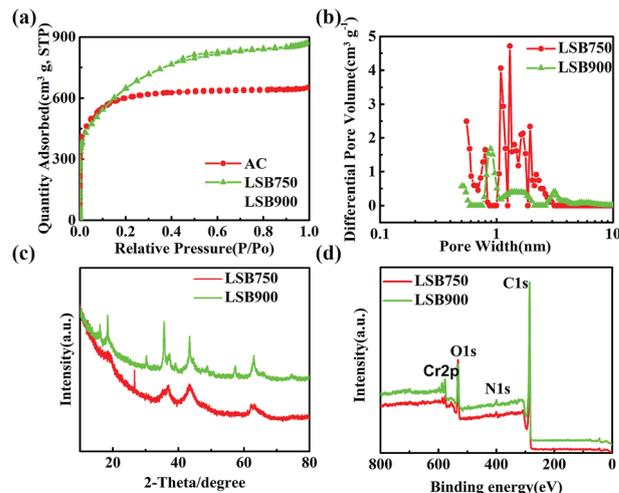

Fig. 2 (a) N_2 adsorption/desorption isotherms, (b) pore size distributions (PSD), (c) XRD measurements, and (d) XPS spectra of LSB.

had occurred, indicating the existence of mesopores.[31] Based on Table 1, BET surface areas followed the trend of AC < LSB750 < LSB900, while the specific surface area of LSB900 was high (up to 2365.00 m^2 g^{-1}). Additionally, when LSB900 and AC have approximately the same micropore surface area, micropore volume, and average pore diameter, the only difference between them is in the external surface area, which suggests that mesopores are more conducive to adsorption of CR. Pore size distribution (PSD) analysis (Fig. 2b) reveals that the LSBs have a micro-/mesoporous structure. The micropores and small mesopores are generated from KOH activation.[32] PSD analysis of AC is shown in Fig. S2b.† As shown in Fig. 2c, X-ray diffraction (XRD) results indicated that the surface of LSB contains chromium crystals. The valence state of chromium in the biochar should be trivalent because carbon in biochar is a reducing agent. X-ray photoelectron spectroscopy (XPS) confirms that the elements on the LSB surface are C, O, Cr, and N. Hence, biochar is beneficial to the adsorption for CR due to its rich active sites.

Adsorption for CR

Effect of pH on adsorption capacity. As shown in Fig. 3a, changes in q_m at different pH are not significant for AC. However, the pH of the CR solution had an influence on CR adsorption of biochar. Adsorption of CR by LSB900 increased from pH 6.0 to 8.0 and then declined slightly from pH 8.0 to 10.0. The adsorption capacity of LSB750 reached a peak value at pH 7.0 with a similar trend as LSB900, except for the slight difference at pH 8.0. As the dye solution is neutralized by positive ions, a significant difference between adsorption abilities of LSB750 and LSB900 is observed. The adsorption capacity for CR of LSB900 is higher than that of LSB750, and both are higher than that of AC. The adsorption capacity for CR of AC in this experiment is higher than the calculated q_m because the initial solution concentration was kept much higher than q_m to show diffusion mechanism. However, in approximately neutral pH, weight loss of chromium in the biochar reached

Table 1 Results of nitrogen adsorption–desorption analysis for the adsorbents

Adsorbents	$S_{BET}{}^{a}$ (m² g⁻¹)	$S_{micro}{}^{b}$ (m² g⁻¹)	$V_{micro}{}^{c}$ (cm³ g⁻¹)	$D_{p}{}^{d}$ (nm)
AC	1221.67	714.48	0.37	2.24
LSB750	1974.12	1023.87	0.51	2.04
LSB900	2365.00	823.27	0.34	2.28

[a] S_{BET}: specific surface area. [b] S_{micro}: micropore surface area. [c] V_{micro}: micropore volume. [d] D_{p}: average pore diameter.
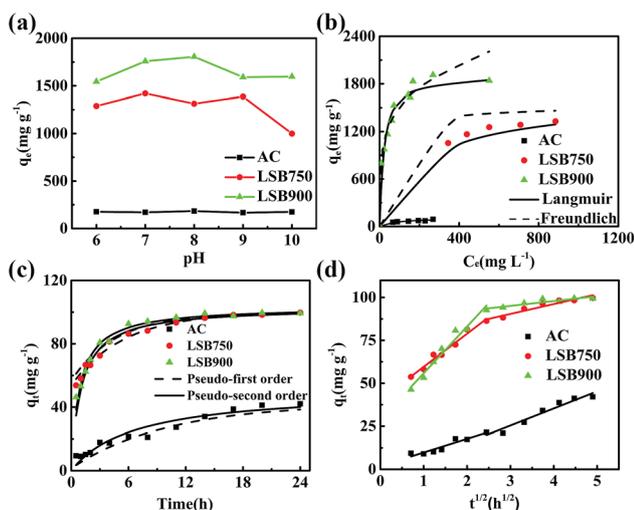
Fig. 3 (a) Effect of aqueous pH; plot of (b) Langmuir and Freundlich isotherm models, (c) pseudo-first order and pseudo-second order kinetics, and (d) intraparticle diffusion kinetics for adsorption capacity of the adsorbents towards CR.

a minimum value (0.008 mg⁻¹ L), which is below the maximum allowable emission standard of total chromium (2 or 5 mg L⁻¹) in surface water.[28,33,34] As pH of CR solution is at ∼7.0,[35] the following experiment was performed without adjusting the pH of aqueous solution.

Adsorption isotherms

Two adsorption models of Langmuir and Freundlich were employed to evaluate the adsorption isotherms of the adsorbents for CR adsorption. The related parameters were calculated by regression analyses, as shown in Table 2, and the plot of q_e versus C_e for the adsorption of CR onto adsorbents at 30 °C is shown in Fig. 3b. Maximum adsorption capacity of LSBs for CR increases with the increase in carbonization temperature, and the adsorption capacity of the LSB is much higher than that of

AC. The q_m values of the state-of-the-art adsorbents are listed in Table 3, showing that the LSBs have comparative high adsorption capacities for CR. The q_m values for LSB750 and LSB900 are ∼18 (1594.79 mg g⁻¹) and ∼22 times (1916.56 mg g⁻¹) higher than that for AC (85.32 mg g⁻¹), respectively. By comparing their correlation coefficient (R^2) values (Table 2), it is more reasonable to describe these adsorption isotherms by the Langmuir isotherm model. The Langmuir isotherm model demonstrates that the removal of CR on LSB is more likely monolayer adsorption. According to BET results of these carbon materials, the increase in surface area from AC to LSB750 is much higher than that from LSB750 to LSB900. The changes in adsorption capacity follow a similar trend, which suggests that chemisorption would be the main driving force for the removal of CR.

Therefore, the adsorption of CR onto the LSB might be due to (1) active sites formed during the carbonization process, (2) high specific surface area from the porous structure of LSB, and (3) chemical bonding between chromium compounds and CR.

Adsorption kinetics

Fig. 3c and Table 4 present plots and parameters of the pseudo-first order and pseudo-second order kinetics of CR adsorption. Higher R^2 value of pseudo-second order model for LSB indicates the existence of chemisorption in the adsorption process.[36] On the contrary, the adsorption ability of AC effectively fits pseudo-first order model. The adsorption equilibrium time of LSBs is about 24 h, which is shorter than that of AC.

Intraparticle diffusion model was also investigated to identify the diffusion mechanism and rate controlling process.[17] As shown in Fig. 3d and Table 5, the plots of q_t versus $t^{1/2}$ for all adsorbents were not linear over the entire time range, and can be separated into two linear regions. This indicates that two functional modes exist in the adsorption of CR on LSB.[37] The first linear plot might be because of external surface adsorption, in which CR diffuses through the aqueous phase to the external surface of adsorbent, and the adsorption rate is high. UV-visible absorption spectra recorded after 4 h adsorption time of the absorbents for CR (200 ppm), as shown in the Fig. S3a,† reveals

Table 2 Langmuir and Freundlich model parameters for adsorption of CR by adsorbents

Adsorbents	Langmuir isotherm			Freundlich isotherm		
	q_m (mg g⁻¹)	k_L (L mg⁻¹)	R^2	k_F (mg g⁻¹)	n	R^2
AC	85.32	0.026	0.9831	14.19	3.18	0.8387
LSB750	1594.79	0.048	0.9870	309.63	4.61	0.8878
LSB900	1916.56	0.050	0.9963	541.13	4.49	0.9031

Table 3 Congo red adsorption capacities on various adsorbents

Adsorbents	Adsorption capacity (mg g^{-1})	Reference
Hierarchical porous ZnO–Al$_2$O$_3$ microspheres	397	40
Mesoporous ZrO$_2$ fiber	103.46	41
Hierarchical flower-like nickel(II) oxide microspheres	534.8	42
Hierarchical bristle-grass-like NH$_4$Al(OH)$_2$CO$_3$@Ni(OH)$_2$	426	43
Porous Fe(OH)$_3$@cellulose hybrid fibers	689.65	13
CaCO$_3$ microspheres (MSs)	99.6	23
Gold-magnetic nanocomposite loaded on activated carbon	43.88	44
Magnetic mesoporous carbon	445.294	45
Activated carbon electropositive amine	319.39	46
Carbon-containing bone hydroxyapatite	329.0	47
Bamboo hydrochars	33.7	20
Spindle-like boehmites	427.4	48
Korean cabbage	1304	4
LSB900	1916	This work
LSB750	1594	This work

Table 4 Parameters of kinetic models for the adsorption of 100 mg L^{-1} Congo red on adsorbents

Adsorbents	Pseudo-first-order			Pseudo-second-order		
	k_1 (min^{-1})	q_e (mg g^{-1})	R^2	k_2 (g mg^{-1} min^{-1})	q_e (mg g^{-1})	R^2
AC	0.10	40.59	0.9311	3.92×10^3	7.80	0.9102
LSB750	0.19	46.11	0.9865	9.80×10^3	104.17	0.9990
LSB900	0.22	42.73	0.9013	11.30×10^3	121.65	0.9996

that LSB has fast adsorption rate and easily decreases the aqueous CR concentration. Furthermore, SEM images of the adsorbents after adsorption (Fig. S3b–d†) showed rough surfaces, suggesting the adsorption of CR on the external surface in low concentrations. The second linear region refers to the gradual adsorption stage, in which the intraparticle diffusion starts to slow down and plateau because intraparticle diffusion is limited by the maximum system adsorption capacity.[37–39] Two processes of adsorption and different linear plots indicate that the speed of CR uptake is related to the specific surface area of the adsorbent.[38] However, the two plot regions for adsorption of AC are similar, which indicates that AC might have only one mode of CR adsorption.

Adsorption thermodynamics

Temperature is an important factor for adsorption. As temperature increases, the rate of diffusion of adsorbate molecules across the external boundary layer and internal pores of the adsorbent particles increases.[49] Thermodynamic parameters

(Table 6), including adsorption free energy (ΔG), adsorption enthalpy (ΔH) and adsorption entropy (ΔS) are calculated by the following eqn (7) and (8):

$$\Delta G = -RT \ln k_0 \qquad (7)$$

$$\ln k_0 = -\Delta H/RT + \Delta S/R \qquad (8)$$

where k_0 is the adsorption equilibrium constant, which is the ratio of the equilibrium concentration of the dye ions on adsorbents to the equilibrium concentration of the dye ions in solution. R (8.314 J mol^{-1} K^{-1}) is universal gas constant and T (K) is temperature. Plot of ln k_0 versus $1/T$ should give a linear line, where values of ΔH (kJ mol^{-1}) and ΔS (J mol^{-1} K^{-1}) can be calculated from the slope and intercept of van't Hoff plots, respectively.

Negative values of ΔG indicate that adsorption of CR on the adsorbents is spontaneous, while positive ΔH values indicate the endothermic nature of the adsorption.[17,50] This further confirms that the adsorption of CR on the LSBs was not only a physical

Table 5 Kinetic constants of intraparticle diffusion model for the adsorption of Congo red on adsorbents

Adsorbents	k_{i1}	I_1	R^2	k_{i2}	I_2	R^2
AC	7.94	1.82	0.8888	9.93	−4.37	0.9409
LSB750	19.29	40.29	0.9707	5.76	73.11	0.9200
LSB900	27.22	28.61	0.9617	2.82	86.63	0.7993

Table 6 Thermodynamic parameters for the adsorption of CR on adsorbents at different temperatures

Adsorbents	−ΔG (kJ mol^{-1})			ΔH (kJ mol^{-1})	ΔS (J mol^{-1} k^{-1})
	303 K	313 K	323 K		
AC	1.16	1.92	2.67	21.74	75.57
LSB750	3.72	4.55	5.40	21.74	84.02
LSB900	4.33	4.78	5.23	9.26	44.84

adsorption process, but also a chemical adsorption process.[20] Positive ΔS values indicate the increased randomness at the adsorbent/solution interface during adsorption for Congo red.

Possible adsorption mechanisms

FT-IR spectra of biochar, biochar-CR and CR (Fig. 4a and b) were analysed to identify the prevailing chemical bond transformations between CR and surface of the adsorbents. Biochar-CR was treated with ethanol prior to analysis. As shown in Fig. 4a, peaks of biochar-CR at 2908, 1223, 1056 and 800–500 cm^{-1} reveal a reduced intensity of adsorption compared to that of biochar.[17] This result conforms to the study reported by Yang *et al.*,[16] which clearly indicates the existence of chemical adsorption in this adsorption process. In addition, the peaks at 3432 cm^{-1} (Fig. 4a) and 3467 cm^{-1} (Fig. 4b) indicate stretching vibration of O–H of biochar before adsorption and N–H of CR, respectively.[51,52] The peak of biochar-CR was broadened, which indicated that hydrogen bonds form between the O–H groups of biochar and the –NH$_2$ groups of CR.[13] In other words, CR adsorption on LSB occurs *via* chemical

adsorption. XPS measurements were also performed on biochar-CR (Fig. 4c and d). Based on Table 7, C contents of biochar increased, while O contents decreased, with the increase in carbonization temperature. This result indicated that dehydration and decarboxylation possibly occurred with the increase in carbonization temperature during the carbonization process.[53] Cr contents are 4.556 and 7.439 wt% for LSB750 and LSB900, respectively. The increase in Cr contents of biochar shows that chromium compound residue increased with the increase in carbonization temperature from 750 °C to 900 °C. Moreover, after adsorption, Cr contents do not change significantly, which shows the stability of biochar in aqueous medium.

Due to –N=N– and –SO$_3^-$ groups of CR (Scheme 1), the increase in N and S contents of LSB after adsorption illustrates the effective removal of CR. Taking the Cr2p$_{3/2}$ curve as an example for LSB750 and LSB900 (Fig. 4c and d, respectively), the peak observed at around 576.6 eV corresponds to the characteristic binding energy of Cr^{3+} species.[54–56] After adsorption, this peak shifted in Cr2p spectra, and binding energy peaks of both LSB750 (Fig. 4c) and LSB900 (Fig. 4d) decreased by 0.44–0.6 eV, although the error in XPS measurements is about 0.2 eV.[57] That indicates that the formation of new bonds occurred. Considering the introduction of CR, the most possible new bond can be Cr–N, whose corresponding peak is located at around 574.8 or 575.8 eV.[58] This conforms to the decrease in binding energy of LSB before and after adsorption due to a chemical reaction between Cr and CR. This result clearly conforms to a new peak at around 166.8 eV, assigned to S2p after adsorption (Fig. 4e).[13]

Furthermore, we found that the adsorption capacity of LSB for Methyl orange (MO, Scheme 2 and Fig. S4†), which also has –N=N– and –SO$_3^-$ groups, is lower than that for CR. However, AC has higher adsorption capacity for MO (Table 8) than for CR. Comparison of adsorption capacities of LSBs and AC along with structures of CR and MO show that –NH$_2$ groups of CR might be a significant factor towards improvement of the CR adsorption capacity of biochar. This again shows the possibility of a reaction between chromium of biochar and –NH$_2$ groups of CR.

After adsorption, we calcined the adsorbents at 350 °C for 3 h to remove CR. As shown in Fig. 4f, after five times recycling, the adsorption capacity of LSBs decreased but is still higher than that of AC, which changes only slightly. This also proves that the interaction between chromium and –NH$_2$ groups on CR is chelation,[27] which cannot be broken by calcination at low temperatures.

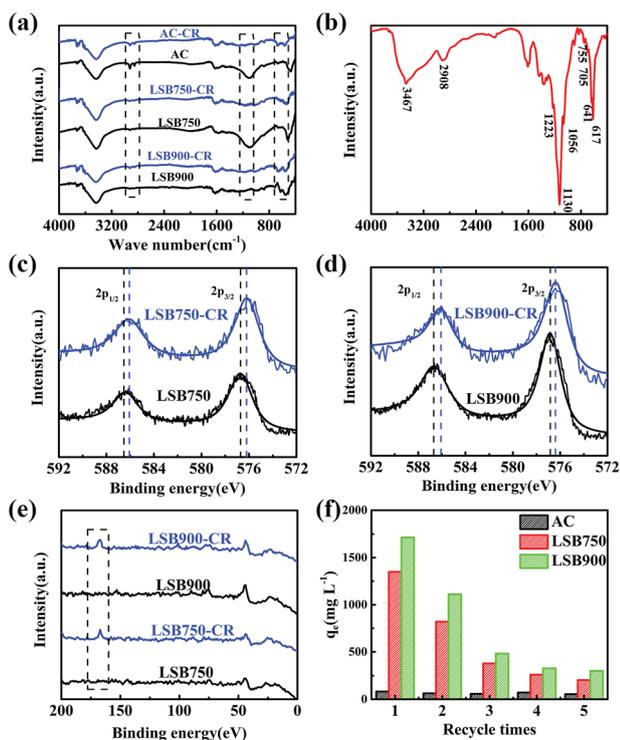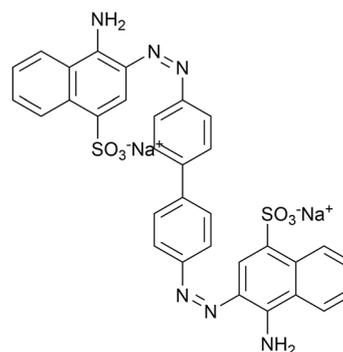**Fig. 4** FT-IR spectra of (a) adsorbents and adsorbents-CR, (b) Congo red; XPS spectra of Cr2p from (c) LSB750 and LSB750-CR, (d) LSB900 and LSB750-CR; (e) total XPS spectra of S2p of LSB; and (f) five time recycling of the adsorbents for CR.
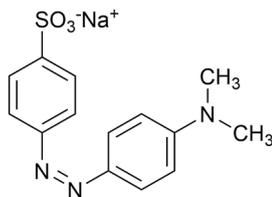

Scheme 1 Molecular structure of Congo red.

Table 7 Elemental compositions of adsorbents and adsorbents-CR

Sample (wt%)	C1s	N1s	O1s	Cr2p	S2p
LSB750	74.504	1.557	19.382	4.556	—
LSB750-CR	70.082	5.273	18.343	4.838	1.465
LSB900	75.738	2.667	14.156	7.439	—
LSB900-CR	70.220	5.242	15.409	7.451	1.678

Scheme 2 Molecular structure of Methyl orange.

Table 8 Langmuir parameters for adsorption of MO by adsorbents

| Adsorbents | Langmuir isotherm | | |
	q_m (mg g^{-1})	k_L (L mg^{-1})	R^2
AC	420.17	−0.0178	0.9946
LSB750	729.93	0.0227	0.9953
LSB900	847.46	0.0291	0.9995

Overall, based on results described above, a possible adsorption mechanism of CR on LSB was deduced. When CR molecules come in contact with the adsorbent surface, the high specific surface area of biochar provides rich active sites. Electrostatic interactions occurred between biochar and –NH$_2$ groups of CR molecules. Moreover, the chelation between chromium compounds and –NH$_2$ groups of CR molecules also manifested a significant impact on adsorption capacity for CR.

Conclusions

In summary, leather shavings biochar (LSB) derived from leather shavings has a high adsorption capacity for CR. LSB exhibited a porous structure with a large specific surface area. A high CR adsorption capacity of 1916 mg g^{-1} was achieved at neutral pH conditions at 30 °C. Through adsorption kinetics and mechanism investigations, it was revealed that biochar essentially immobilized the dye via chelation between the chromium compounds and –NH$_2$ of CR and electrostatic interactions. Therefore, the nature of the removal of CR is a combination of physical and chemical adsorption. This biochar proved to be a simple, highly efficient, inexpensive and environmentally-friendly material, which has potential for versatile applications.

Conflicts of interest

There are no conflicts to declare.

Acknowledgements

References

1 Y. D. Chen, Y. C. Lin, S. H. Ho, Y. Zhou and N. Q. Ren, *Bioresour. Technol.*, 2018, **259**, 104–110.
2 K. B. Tan, M. Vakili, B. A. Horri, P. E. Poh, A. Z. Abdullah and B. Salamatinia, *Sep. Purif. Technol.*, 2015, **150**, 229–242.
3 S. Chatterjee, D. S. Lee, M. W. Lee and S. H. Woo, *Bioresour. Technol.*, 2009, **100**, 2803.
4 D. D. Sewu, P. Boakye and S. H. Woo, *Bioresour. Technol.*, 2017, **224**, 206.
5 H. Patel and R. T. Vashi, *J. Saudi Chem. Soc.*, 2012, **16**, 131–136.
6 Q. W. Cao, Y. F. Zheng, H. Y. Yin and X. C. Song, *J. Mater. Sci.*, 2016, **51**, 4559–4565.
7 M. Chafi, B. Gourich, A. H. Essadki, C. Vial and A. Fabregat, *Desalination*, 2011, **281**, 285–292.
8 L. Fan, Y. Zhou, W. Yang, G. Chen and F. Yang, *Dyes Pigm.*, 2008, **76**, 440–446.
9 Y. Omidi Khaniabadi, H. Basiri, H. Nourmoradi, M. J. Mohammadi, A. R. Yari, S. Sadeghi and A. Amrane, *Int. J. Chem. React. Eng.*, 2018, **16**, DOI: 10.1515/ijcre-2016-0203.
10 J. Zhang, X. Yan, M. Hu, X. Hu and M. Zhou, *J. Mol. Liq.*, 2018, **249**, 772–778.
11 X. Luo, H. Liang, F. Qu, A. Ding, X. Cheng, C. Y. Tang and G. Li, *Chemosphere*, 2018, **200**, 237–247.
12 Y.-Y. Chen, S.-H. Yu, H.-F. Jiang, Q.-Z. Yao, S.-Q. Fu and G.-T. Zhou, *Appl. Surf. Sci.*, 2018, **444**, 224–234.
13 J. Zhao, Z. Lu, X. He, X. Zhang, Q. Li, T. Xia, W. Zhang and C. Lu, *ACS Sustainable Chem. Eng.*, 2017, **5**, 7723–7732.
14 X. Luo, J. Zeng, S. Liu and L. Zhang, *Bioresour. Technol.*, 2015, **194**, 403–406.
15 S. P. Sohi, E. Krull, E. Lopez-Capel and R. Bol, *Adv. Agron.*, 2010, **105**, 47–82.
16 G. Yang, L. Wu, Q. Xian, F. Shen, J. Wu and Y. Zhang, *PLoS One*, 2016, **11**, e0154562.
17 X. Liu, J. Sun, S. Duan, Y. Wang, T. Hayat, A. Alsaedi, C. Wang and J. Li, *Sci. Rep.*, 2017, **7**, 10033.
18 K. R. Thines, E. C. Abdullah and N. M. Mubarak, *Microporous Mesoporous Mater.*, 2017, **253**, 29–39.
19 J. Jang, W. Miran, S. D. Divine, M. Nawaz, A. Shahzad, S. H. Woo and D. S. Lee, *Sci. Total Environ.*, 2018, **615**, 698–707.
20 Y. Li, A. Meas, S. Shan, R. Yang and X. Gai, *Bioresour. Technol.*, 2016, **207**, 379–386.
21 A. W. Samsuri, F. Sadegh-Zadeh and B. J. Seh-Bardan, *Int. J. Environ. Sci. Technol.*, 2014, **11**, 967–976.
22 Y. Zhu, B. Yi, Q. Yuan, Y. Wu, M. Wang and S. Yan, *RSC Adv.*, 2018, **8**, 19917–19929.
23 M. Zhao, Z. Chen, X. Lv, K. Zhou, J. Zhang, X. Tian, X. Ren and X. Mei, *R. Soc. Open Sci.*, 2017, **4**, 170697.
24 M. Hu, X. Yan, X. Hu, J. Zhang, R. Feng and M. Zhou, *J. Colloid Interface Sci.*, 2018, **510**, 111–117.
25 H. Chen, J. Luo, X. Wang, X. Liang, Y. Zhao, C. Yang, M. I. Baikenov and X. Su, *Microporous Mesoporous Mater.*, 2018, **255**, 69–75.
26 D. Sud, G. Mahajan and M. P. Kaur, *Bioresour. Technol.*, 2008, **99**, 6017–6027.
27 Z. Li, T. Li, L. An, H. Liu, L. Gu and Z. Zhang, *Colloids Surf., A*, 2016, **494**, 65–73.

28 D. Zhao, X. Gao, C. Wu, R. Xie, S. Feng and C. Chen, *Appl. Surf. Sci.*, 2016, **384**, 1–9.

29 Y. Yang, G. Wang, B. Wang, Z. Li, X. Jia, Q. Zhou and Y. Zhao, *Bioresour. Technol.*, 2011, **102**, 828–834.

30 K. S. W. Sing, *Pure Appl. Chem.*, 1985, **57**, 603–619.

31 C. Li, L. Zhang, H. Xia, J. Peng, S. Zhang, S. Cheng and J. Shu, *J. Mol. Liq.*, 2016, **224**, 737–744.

32 H. Shao, F. Ai, W. Wang, H. Zhang, A. Wang, W. Feng and Y. Huang, *J. Mater. Chem. A*, 2017, 19892–19900.

33 A. El Nemr, A. El-Sikaily, A. Khaled and O. Abdelwahab, *Arabian J. Chem.*, 2015, **8**, 105–117.

34 A. B. Albadarin, C. Mangwandi, A. a. H. Al-Muhtaseb, G. M. Walker, S. J. Allen and M. N. M. Ahmad, *Chem. Eng. J.*, 2012, **179**, 193–202.

35 H. Chen, Y. Zheng, B. Cheng, J. Yu and C. Jiang, *J. Alloys Compd.*, 2018, **735**, 1041–1051.

36 Y. S. Ho, *J. Hazard. Mater.*, 2006, **136**, 681–689.

37 Z. Hu, H. Chen, F. Ji and S. Yuan, *J. Hazard. Mater.*, 2010, **173**, 292–297.

38 E. Lorencgrabowska and G. Gryglewicz, *Dyes Pigm.*, 2007, **74**, 34–40.

39 S. H. Kim and P. P. Choi, *Dalton Trans.*, 2017, **46**, 15470–15479.

40 C. Lei, M. Pi, D. Xu, C. Jiang and B. Cheng, *Appl. Surf. Sci.*, 2017, **426**, 360–368.

41 Z. Yu, B. Liu, H. Zhou, C. Feng, X. Wang, K. Yuan, X. Gan, L. Zhu, G. Zhang and D. Xu, *Appl. Surf. Sci.*, 2017, **399**, 288–297.

42 Y. Zheng, B. Zhu, H. Chen, W. You, C. Jiang and J. Yu, *J. Colloid Interface Sci.*, 2017, **504**, 688–696.

43 Y. Zheng, H. Wang, B. Cheng, W. You and J. Yu, *J. Alloys Compd.*, 2018, **750**, 644–654.

44 E. A. Dil, M. Ghaedi, A. Asfaram and A. A. Bazrafshan, *Ultrason. Sonochem.*, 2018, **46**, 99–105.

45 H. S. Saroyan, D. A. Giannakoudakis, C. S. Sarafidis, N. K. Lazaridis and E. A. Deliyanni, *J. Chem. Technol. Biotechnol.*, 2017, **92**, 1899–1911.

46 C. Tian, C. Feng, M. Wei and Y. Wu, *Chemosphere*, 2018, **208**, 476–483.

47 Q. Peng, F. Yu, B. Huang and Y. Huang, *RSC Adv.*, 2017, **7**, 26968–26973.

48 G. Li, Y. Sun, X. Li and Y. Liu, *RSC Adv.*, 2016, **6**, 11855–11862.

49 R. Jain and S. Sikarwar, *J. Hazard. Mater.*, 2008, **152**, 942–948.

50 Y. Chen, M. He, C. Wang and Y. Wei, *J. Mater. Chem. A*, 2014, **2**, 10444.

51 Z.-L. Wu, F. Liu, C.-K. Li, X.-Q. Chen and J.-G. Yu, *Colloids Surf., A*, 2016, **509**, 65–72.

52 K. K. Sadasivuni, A. Kafy, L. Zhai, H. U. Ko, S. Mun and J. Kim, *Small*, 2015, **11**, 994–1002.

53 M. Keiluweit, P. S. Nico, M. G. Johnson and M. Kleber, *Environ. Sci. Technol.*, 2010, **44**, 1247–1253.

54 B. Liu, H. Nakatani and M. Terano, *J. Mol. Catal. A: Chem.*, 2002, **184**, 387–398.

55 J. Fang, Z. Gu, D. Gang, C. Liu, E. S. Ilton and B. Deng, *Environ. Sci. Technol.*, 2007, **41**, 4748–4753.

56 G. Cappelletti, C. L. Bianchi and S. Ardizzone, *Appl. Catal., B*, 2008, **78**, 193–201.

57 C. Uebing, H. Viefhaus and H. J. Grabke, *Appl. Surf. Sci.*, 1988, **32**, 363–380.

58 X. S. Wan, S. S. Zhao, Y. Yang, J. Gong and C. Sun, *Surf. Coat. Technol.*, 2010, **204**, 1800–1810.